LA-UR-18-24093 (Accepted Manuscript)

A crystal plasticity model for body-centered cubic molybdenum: Experiments and simulations

Daphalapurkar, Nitin Pandurang
Patil, Swapnil
Nguyen, Thao
Eswar Prasad, Korimilli
Ramesh, Kaliat

Provided by the author(s) and the Los Alamos National Laboratory (2019-02-05).

To be published in: Materials Science and Engineering: A

DOI to publisher's version: 10.1016/j.msea.2018.09.099

Permalink to record: http://permalink.lanl.gov/object/view?what=info:lanl-repo/lareport/LA-UR-18-24093

Disclaimer:
Approved for public release. Los Alamos National Laboratory, an affirmative action/equal opportunity employer, is operated by the Los Alamos National Security, LLC for the National Nuclear Security Administration of the U.S. Department of Energy under contract DE-AC52-06NA25396. Los Alamos National Laboratory strongly supports academic freedom and a researcher's right to publish; as an institution, however, the Laboratory does not endorse the viewpoint of a publication or guarantee its technical correctness.

Author's Accepted Manuscript

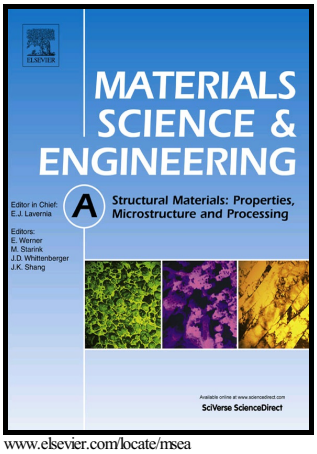

www.elsevier.com/locate/msea

A Crystal Plasticity Model for Body-centered Cubic Molybdenum: Experiments and Simulations

Nitin P. Daphalapurkar, Swapnil Patil, Thao Nguyen, Korimilli Eswar Prasad, Kaliat T. Ramesh

PII: S0921-5093(18)31308-X
DOI: https://doi.org/10.1016/j.msea.2018.09.099
Reference: MSA36980

To appear in: *Materials Science & Engineering A*

Received date: 11 May 2018
Accepted date: 26 September 2018

Cite this article as: Nitin P. Daphalapurkar, Swapnil Patil, Thao Nguyen, Korimilli Eswar Prasad and Kaliat T. Ramesh, A Crystal Plasticity Model for Body-centered Cubic Molybdenum: Experiments and Simulations, *Materials Science & Engineering A,* https://doi.org/10.1016/j.msea.2018.09.099

This is a PDF file of an unedited manuscript that has been accepted for publication. As a service to our customers we are providing this early version of the manuscript. The manuscript will undergo copyediting, typesetting, and review of the resulting galley proof before it is published in its final citable form. Please note that during the production process errors may be discovered which could affect the content, and all legal disclaimers that apply to the journal pertain.

ACCEPTED MANUSCRIPT

A Crystal Plasticity Model for Body-centered Cubic Molybdenum: Experiments and Simulations

Nitin P. Daphalapurkar

Theoretical Division, Los Alamos National Laboratory
P.O. Box 1663, MS B216, Los Alamos, NM 87545, U.S.A.

Swapnil Patil

General Electric Global Research Center
Bangalore, India

Thao Nguyen

Department of Mechanical Engineering, Texas A&M University
College Station, TX 77843, U.S.A.

Korimilli Eswar Prasad

Department of Metallurgy and Materials Science, Indian Institute of Technology
Indore 453552, India

Kaliat T. Ramesh

Department of Mechanical Engineering, The Johns Hopkins University
3400 N Charles St, Baltimore, MD 21218, U.S.A.

Accepted manuscript

Abstract

A physics-based finite strain crystal plasticity constitutive model for body-centered-cubic (BCC) single crystals is developed to capture the strong temperature, rate and orientation dependence of mechanical behavior. The key features of the model include twinning-anti-twinning asymmetry of shearing resistance, a yield criterion that incorporates atomistics-informed non-Schmid effects, and a flow rule formulated based on the theory of thermally activated motion of screw dislocations via nucleation of double kinks. The implementation of the constitutive model in a finite-element program is briefly discussed. The material constants in the model are determined by calibrating the model against literature-based experimental data on single-crystal

ACCEPTED MANUSCRIPT

Molybdenum subjected to uniaxial compression and uniaxial tension. Experiments of uniaxial compression on a single crystal specimen with a hole were performed for validation of the calibrated model for BCC Molybdenum. Measurements of deformations in the vicinity of the hole were used to assess the ability of the model in predicting localized deformation patterns around the hole. The model is able to effectively describe the anisotropic and temperature-dependent stress-strain response of a molybdenum crystal up to a homologous temperature of 0.3.

Keywords: BCC Crystal plasticity, Thermal activation, Non-Schmid effects, Molybdenum single crystal, Finite elements

Accepted manuscript

1. Introduction

The body-centered cubic (BCC) transition metals have a complex deformation behavior, a large part of which can be attributed to their lattice crystallography. Among these characteristic behaviors are the strong temperature, rate and orientation dependence of yield stress as well as asymmetry with respect to tension and compression. It is known that the room temperature plasticity of BCC metals is controlled, to a large extent, by the motion of screw dislocations (Taylor (1992)). The connection between the details of core structure and mobility of screw dislocations in BCC metals has been extensively studied using atomistic simulations, e.g. Ito and Vitek (2001). In this work, the major results from these atomistic calculations are systematically transferred to the macroscopic level while formulating a finite strain continuum crystal plasticity model for BCC single crystals.

Both atomistic and ab-initio simulations (Vitek, 1976; Woodward and Rao, 2001) showed that a screw dislocation in BCC metals has a complex non-planar atomic core structure. Consequently, the flow stress increases rapidly with decreasing temperature and increasing strain rate. Further, such a core structure is also responsible for breakdown of the Schmid law which leads to complex dependence of yield stress on orientation of loading.

The non-planar cores of screw dislocations gives them lower mobility than dislocations of edge character. The low mobility of screw dislocations is therefore expected to control the plastic flow in BCC metals. The motion of screw dislocations occurs through the nucleation and the propagation of double-kinks along their lines (Kocks et al., 1975; Tang et al., 1998). The double-kink mechanism is a thermally activated process, which explains the

ACCEPTED MANUSCRIPT

strong temperature dependence of the flow stress observed in BCC metals. In the model presented in this paper, thermally activated dislocation mobility theory is adopted to describe the shearing rate on slip systems.

Atomistic molecular dynamics simulations (Ito and Vitek, 2001; Vitek et al., 2004a,b) have shown that the response of the screw dislocation core to an externally applied stress state is very complex. The critical resolved shear stress (CRSS) is affected not only by the usual (Schmid) resolved shear stress on the dislocation, but also by non-driving stress components. Consequences of the latter are referred to as non-Schmid effects. In particular, Ito and Vitek (2001) have shown that the shear stresses both parallel and perpendicular to the Burgers vector that act not only in the slip plane but in all three $\{110\}$ and $\{112\}$ planes of the $\langle 111 \rangle$ zone can either increase or decrease the degree of core spreading on non-slip planes. This in turn, increases or decreases the CRSS on the slip plane. Such atomic-scale phenomena are expected to significantly affect the plastic behavior of BCC crystals and in particular lead to a strong orientation-dependence of CRSS and tension-compression asymmetry. In this paper, a yield criterion that incorporates atomistics-informed non-Schmid effects is adopted.

The identification of the active slip plane and slip mechanism is much more complicated in BCC metals than in FCC metals. In BCC metals, the deformation occurs by crystallographic planes sliding parallel to the $\langle 111 \rangle$ axis (which is the direction of closest atomic packing) but unlike in FCC materials, the slip plane is not well-defined. Taylor and Elam (1926) proposed the concept of pencil glide, which implied that any plane of the zone defined by the operating $\langle 111 \rangle$ slip direction might act as slip plane. However, later research (Hollang et al., 1997; Seeger, 2001, 2004; Seeger and Wasserbach, 2002) concluded that $\{110\}$, $\{112\}$ and $\{123\}$ families of planes primarily participate in the slip process during deformation of BCC metals. This indicates that the operating slip plane is not necessarily those with the densest packing, and must be determined experimentally as functions of crystal orientation, temperature, purity, etc. (Seeger, 2001, 2004) and (Seeger and Wasserbach, 2002) noted that at low-temperature ($< 75K$) slip takes place predominantly on $\{110\}$ planes, but not necessarily at higher temperatures. They further argued that purer materials do not show $\{123\}$ slip and that substitutional impurities had presumably been responsible for the slip on $\{123\}$ planes reported earlier. In summary, for high-purity BCC metals it suffices to take into account $\{110\}$ and $\{112\}$ slip planes. In this work, attention is focused on deformation behavior of BCC metals at room temperature

Accepted manuscript

ACCEPTED MANUSCRIPT

and above (up to homologous temperature ≤ 0.3). Therefore, we develop a model for BCC metals that deform by $\{110\}$ and $\{112\}$ slip.

In spite of the fact that several investigations were dedicated to study the response of BCC polycrystals using crystal plasticity based models, no explicit efforts were made to simulate the response of BCC single crystals accurately. (Liao et al., 1998) and (Lee et al., 1999) extended the crystal plasticity framework developed for FCC material, which is based on power-law descriptions (Peirce et al., 1983) for shearing rates, to model BCC materials. Although power-law relations offer simple approximations of the viscoplastic response, they cannot capture the temperature and rate dependence of critical resolved shear stress observed in BCC crystals. Kothari and Anand (1998); Xie et al. (2004), and Ganapathysubramanian and Zabaras (2005) used a kinetic equation for the shearing rates on slip systems based on the thermally activated theory of plastic flow. However, their formulation does not consider non-Schmid behaviors responsible for the strong orientation-dependence of CRSS and tension-compression asymmetry. This paper seeks to develop a rigorous continuum crystal plasticity constitutive model for BCC metals that captures correctly thermally activated plastic flow, the breakdown of the Schmid law and the twinning-anti-twinning asymmetry of shearing resistance.

Yalcinkaya et al. (2008) performed material point calculations for different BCC crystals subjected to uniaxial tension loading and determined their material properties using a least-square optimization procedure. Their material point implementation is based on the predefined uniaxial deformation gradient, as opposed to finite element implementation in which the deformation gradient is determined from the applied boundary conditions. Since, the predefined uniaxial deformation gradient may not be representative of the experimental loading (e.g. Poisson strains may not be captured correctly), a finite element implementation is used in this work to study response of BCC crystals and determine the material properties.

The objective of this paper is to develop a physics based finite strain continuum crystal plasticity constitutive model for BCC single crystals that captures the strong temperature, rate- and orientation-dependence of yield stress as well as the twinning-anti-twinning asymmetry of shearing resistance. To this end, the flow rule is derived from the theory of thermally activated motion of screw dislocations via nucleation of double kinks. A yield criterion that incorporates atomistically informed non-Schmid effects is used in the model (section 2). A second objective of the work is to implement the above

Accepted manuscript

ACCEPTED MANUSCRIPT

constitutive model in a finite element framework. This task is accomplished in section 3 by employing the rate tangent modulus scheme and finite element formulation for incremental static equilibrium. The last objective of this work is to provide a systematic two step procedure for determining the required material properties with minimal compromise of their physical interpretation. To this end, the constitutive model presented in this paper is applied to a molybdenum single crystal in section 4 and its behavior at different orientations and temperatures is simulated.

2. Finite deformation theory of crystal plasticity

The general framework of finite strain single crystal plasticity theory, discussed in detail by (Asaro, 1983), is adopted in this work to model the constitutive behavior of BCC crystals.

2.1. Kinematics

The deformation gradient $\boldsymbol{F}$ is assumed to decompose multiplicatively, such that,

$$\boldsymbol{F} = \boldsymbol{F}^{*}\boldsymbol{F}^{p}, \tag{1}$$

where $\boldsymbol{F}^{p}$ is the deformation gradient solely due to plastic shearing on crystallographic slip systems and $\boldsymbol{F}^{*}$ is the deformation gradient which arises from the elastic stretching and rotation of the crystal lattice (see, Figure 1). The deformation in Equation (1) can be envisioned as accomplished in two stages: the material first moves through the undeformed crystal lattice via dislocation motion, according to $\boldsymbol{F}^{p}$ and then the lattice itself, with the material embedded on it, undergoes elastic deformation and rotations giving rise to $\boldsymbol{F}^{*}$. In order to link the macroscopic plastic deformation gradient $\boldsymbol{F}^{p}$ to dislocation movement, n slip systems $\alpha = 1, 2, ...n$, defined by pairs $(\boldsymbol{s}^{(\alpha)}, \boldsymbol{m}^{(\alpha)})$ are introduced as shown in Figure 1. For the αth slip system, the unit vector normal to the slip plane in the undeformed configuration is defined by $\boldsymbol{m}^{\alpha}$ and the unit vector along the slip direction by $\boldsymbol{s}^{\alpha}$. When the deformation gradient $\boldsymbol{F}^{*}$ is applied, the crystalline lattice rotates and these vectors transform to $\boldsymbol{m}^{*(\alpha)}$ and $\boldsymbol{s}^{*(\alpha)}$ respectively, in the current configuration (see, Figure 1), according to:

$$\begin{aligned} \boldsymbol{s}^{*(\alpha)} &= \boldsymbol{F}^{*}\boldsymbol{s}^{(\alpha)}, \\ \boldsymbol{m}^{*(\alpha)} &= \boldsymbol{F}^{*^{-T}}\boldsymbol{m}^{(\alpha)}. \end{aligned} \tag{2}$$

Accepted manuscript

ACCEPTED MANUSCRIPT

The form of $\boldsymbol{m}^{*(\alpha)}$ is chosen such that in the current configuration

$$\boldsymbol{s}^{*(\alpha)} \cdot \boldsymbol{m}^{*(\alpha)} = \boldsymbol{s}^{(\alpha)} \cdot \boldsymbol{m}^{(\alpha)} = 0. \tag{3}$$

The spatial velocity gradient is written as

$$\boldsymbol{l} = \dot{\boldsymbol{F}}\boldsymbol{F}^{-1} = \dot{\boldsymbol{F}}^{*}\boldsymbol{F}^{*^{-1}} + \boldsymbol{F}^{*}\dot{\boldsymbol{F}}^{p}\boldsymbol{F}^{p^{-1}}\boldsymbol{F}^{*^{-1}} \triangleq \boldsymbol{l}^{*} + \boldsymbol{l}^{p}. \tag{4}$$

The evolution equation for $\boldsymbol{F}^p$ (flow rule) is written as (Asaro, 1983):

$$\boldsymbol{L}^p = \dot{\boldsymbol{F}}^p\boldsymbol{F}^{p^{-1}} = \sum_{\alpha=1}^{n} \dot{\gamma}^{\alpha}(\boldsymbol{s}^{(\alpha)} \otimes \boldsymbol{m}^{(\alpha)}), \tag{5}$$

where $\dot{\gamma}^{\alpha}$ is the plastic slip rate on slip system α and n is the total number of slip systems. The summation here is due to multiple slip. Thus, it follows from the form of the flow rule that the plastic part of the deformation is volume preserving since

$$\mathrm{trace}(\boldsymbol{l}^p) = \sum_{\alpha=1}^{n} \dot{\gamma}^{\alpha}\mathrm{trace}(\boldsymbol{s}^{*(\alpha)} \otimes \boldsymbol{m}^{*(\alpha)}) = \sum_{\alpha=1}^{n} \dot{\gamma}^{\alpha}(\boldsymbol{s}^{*(\alpha)} \cdot \boldsymbol{m}^{*(\alpha)}) = 0 \tag{6}$$

Hence, the plastic part of the spatial velocity gradient becomes

$$\boldsymbol{l}^p = \boldsymbol{D}^p + \boldsymbol{\Omega}^p = \boldsymbol{F}^{*}\dot{\boldsymbol{F}}^p\boldsymbol{F}^{p^{-1}}\boldsymbol{F}^{*^{-1}} = \sum_{\alpha=1}^{n} \dot{\gamma}^{\alpha}(\boldsymbol{s}^{*(\alpha)} \otimes \boldsymbol{m}^{*(\alpha)}), \tag{7}$$

where the symmetric and skew-symmetric parts of $\boldsymbol{l}^p$ (i.e., plastic parts of rate of deformation and spin) are written as

$$\boldsymbol{D}^p = \sum_{\alpha=1}^{n} \dot{\gamma}^{\alpha}\left(\frac{1}{2}\left(\boldsymbol{s}^{*(\alpha)} \otimes \boldsymbol{m}^{*(\alpha)} + \boldsymbol{m}^{*(\alpha)} \otimes \boldsymbol{s}^{*(\alpha)}\right)\right) \triangleq \sum_{\alpha=1}^{n} \dot{\gamma}^{\alpha}\boldsymbol{\mu}^{(\alpha)}, \tag{8}$$

$$\boldsymbol{\Omega}^p = \sum_{\alpha=1}^{n} \dot{\gamma}^{\alpha}\left(\frac{1}{2}\left(\boldsymbol{s}^{*(\alpha)} \otimes \boldsymbol{m}^{*(\alpha)} - \boldsymbol{m}^{*(\alpha)} \otimes \boldsymbol{s}^{*(\alpha)}\right)\right) \triangleq \sum_{\alpha=1}^{n} \dot{\gamma}^{\alpha}\boldsymbol{\omega}^{(\alpha)}. \tag{9}$$

Accepted manuscript

ACCEPTED MANUSCRIPT

2.2. Constitutive law

2.2.1. Elastic constitutive relation

Assuming that the elastic properties of the lattice are unaffected by slip, the elastic constitutive relation is specified by

$$\overset{\nabla}{\boldsymbol{\tau}}{}^{*} = \boldsymbol{L} : \boldsymbol{D}^{*}. \tag{10}$$

Here, $\boldsymbol{L}$ is the fourth-order tensor of elastic moduli, $\boldsymbol{D}^{*}$ is the symmetric part of $\boldsymbol{l}^{*}$ (i.e., elastic part of rate of deformation) and $\overset{\nabla}{\boldsymbol{\tau}}{}^{*}$ is the Jaumann rate of Kirchhoff stress based on lattice rotations which is given by,

$$\overset{\nabla}{\boldsymbol{\tau}}{}^{*} = \dot{\boldsymbol{\tau}} - \boldsymbol{\Omega}^{*}\boldsymbol{\tau} + \boldsymbol{\tau}\boldsymbol{\Omega}^{*}. \tag{11}$$

where $\dot{\boldsymbol{\tau}}$ is the material time derivative of Kirchhoff stress and $\boldsymbol{\Omega}^{*}$ is the antiosymmetric part of $\boldsymbol{l}^{*}$. One should note that $\overset{\nabla}{\boldsymbol{\tau}}{}^{*}$ is the rate of change of Kirchhoff stress as seen by an observer who rotates with the lattice according to $\boldsymbol{\Omega}^{*}$. The stress rate as seen by an observer rotating according to $\boldsymbol{\Omega}$ is the Jaumann rate of Kirchhoff stress based on material spin, given by,

$$\overset{\nabla}{\boldsymbol{\tau}} = \dot{\boldsymbol{\tau}} - \boldsymbol{\Omega}\boldsymbol{\tau} + \boldsymbol{\tau}\boldsymbol{\Omega}. \tag{12}$$

The difference between the two rates of Kirchhoff stress is given, by virtue of eq(9) as :

$$\overset{\nabla}{\boldsymbol{\tau}}{}^{*} - \overset{\nabla}{\boldsymbol{\tau}} = \sum_{\alpha=1}^{n} \dot{\gamma}^{\alpha}(\boldsymbol{\omega}^{\boldsymbol{\alpha}}\boldsymbol{\tau} - \boldsymbol{\tau}\boldsymbol{\omega}^{\boldsymbol{\alpha}}) \triangleq \sum_{\alpha=1}^{n} \dot{\gamma}^{\alpha}\boldsymbol{\beta}^{\boldsymbol{\alpha}}. \tag{13}$$

The right hand side of above equation vanishes when there is no relative motion of the material and lattice. On combining eq(8), eq(10) and eq(13), one obtains

$$\overset{\nabla}{\boldsymbol{\tau}} = \boldsymbol{L} : \boldsymbol{D} - \sum_{\alpha=1}^{n} \dot{\gamma}^{\alpha}(\boldsymbol{L} : \boldsymbol{\mu}^{(\alpha)} + \boldsymbol{\beta}^{\boldsymbol{\alpha}}) \triangleq \boldsymbol{L} : \boldsymbol{D} - \sum_{\alpha=1}^{n} \dot{\gamma}^{\alpha}\boldsymbol{R}^{\boldsymbol{\alpha}}, \tag{14}$$

where $\boldsymbol{D}$ is symmetric part of $\boldsymbol{l}$.

The resolved shear stress (also called Schmid stress), τ^{α}, is typically assumed to be the driving force for plastic slip γ^{α} on system α. It is a projection

Accepted manuscript

ACCEPTED MANUSCRIPT

of Kirchhoff stress ($\boldsymbol{\tau}$) on the slip plane in the slip direction and is defined as

$$\tau^{\alpha} = \boldsymbol{\tau} : (\boldsymbol{s}^{*(\alpha)} \otimes \boldsymbol{m}^{*(\alpha)}) = \boldsymbol{\tau} : \boldsymbol{\mu}^{(\alpha)}. \tag{15}$$

2.2.2. Plastic slip rate

In order to complete the description of the constitutive law, the shear slip rates, $\dot{\gamma}^{\alpha}$, need to be specified in terms of those quantities which affect the dislocation motion. The motion of dislocations is driven by an applied resolved shear stress (τ^{α}) and is hindered by short-range barriers (e.g. lattice resistance or Peierls stress), which can be overcome by thermal activation as described subsequently, and long range forces (say, other dislocations). The latter may produce barriers too large for thermal activation to be significant. Thus, flow stress consists of two contributions. One is the thermal component ($\tau_{\circ}$) and the other is an athermal component (g^{α}). It has been established that in BCC metals, at low homologous temperatures, the primary barriers to the motion of the screw dislocations are lattice-related Peierls barriers. Therefore, in the present work, a theory of thermally activated motion of screw dislocations via nucleation of double kinks is adopted to derive the expression for plastic slip rate on active slip systems.

We assume that a segment of initially straight screw dislocation overcomes the Peierls barriers by nucleating a well-separated pair of kinks and making a discrete jump as shown in Figure 2. For example, in pure molybdenum at room temperature the velocity of edge dislocations has been estimated to be 40 times that of screw dislocations (Lawley and Gaigher, 1964)). As a result, kinks migrate along the dislocation line and this leads to the effective glide of the screw dislocation in the direction of the kink formation. The effective glide velocity of screw dislocations is thus primarily controlled by the kink pair nucleation rate. The kink pair nucleation being a thermally activated process, its rate follows an Arrhenius law and is given by

$$\nu_k = \nu_{ko} \exp\left(-\frac{\Delta G_k}{\kappa T}\right) \tag{16}$$

where ν_{ko}, κ and T are the attempt frequency, Boltzmann constant and absolute temperature, respectively. ΔG_k is the activation enthalpy (also called the activation barrier) for nucleating a double kink under an applied resolved shear stress. At finite temperatures, the Peierls barrier is overcome partly with the aid of thermal fluctuations and partly by the work done by the

Accepted manuscript

ACCEPTED MANUSCRIPT

applied Schmid stress (τ^α) during the activation process. The activation barrier (ΔG_k) is the fraction of the Peierls barrier that remains after subtracting the work done by the Schmid stress when shifting the dislocation up on the barrier.

The corresponding average dislocation velocity is estimated as

$$\nu_d = \lambda \nu_k = \lambda \nu_{ko} \exp\left(-\frac{\Delta G_k}{\kappa T}\right). \tag{17}$$

Here, λ is the distance between the barriers (in BCC metals of the same order as the Burgers vector). The relation between the slip rate and the average velocity is given by the Orowan relation, $\dot{\gamma^\alpha} = b\rho_m \nu_d$, where ρ_m and b represent the mobile dislocation density and Burgers vector, respectively. Substituting the expression for average dislocation velocity (17) into Orowan's relation, the expression for slip rate becomes

$$\dot{\gamma^\alpha} = \begin{cases} 0 & \text{if } \tau^\alpha_{eff} \leq 0, \\ \dot{\gamma}_\circ \exp\left(-\frac{\Delta G_k}{\kappa T}\right) & \text{if } \tau^\alpha_{eff} > 0, \end{cases} \tag{18}$$

where, $\dot{\gamma}_\circ = b\rho_m \lambda \nu_{ko}$ is a reference strain rate ($\geq 10^6 \text{s}^{-1}$ for BCC metals). The effective resolved shear stress, τ^α_{eff}, is deduced from the Schmid stress, τ^α, by subtracting athermal component (g^α) of the total slip resistance.

$$\tau^\alpha_{eff} = |\tau^\alpha| - g^\alpha \tag{19}$$

It is redefined subsequently in this subsection to accommodate the non-Schmid behavior discussed in the introduction.

The stress dependence of $\dot{\gamma^\alpha}$ arises from the stress dependence of ΔG_k. A common approach to the definition of the dependence of the activation energy ΔG_k on the stress is to use an empirical function first proposed by Kocks et al. (1975):

$$\Delta G_k = \Delta G_{k\circ} \left[1 - \left(\frac{\tau^\alpha_{eff}}{\tau_\circ}\right)^p \right]^q, \tag{20}$$

where, p and q are adjustable parameters and lie in the range $0 \leq p \leq 1$ and $1 \leq q \leq 2$. $\Delta G_{k\circ}$ is the total activation enthalpy necessary to overcome the lattice resistance without the help of external forces. $\tau_\circ$ is the resolved yield stress at 0 K, *i.e.*, the resolved shear stress required to overcome the lattice

Accepted manuscript

ACCEPTED MANUSCRIPT

resistance when no thermal energy is available.

As discussed in the introduction, it is well known that for BCC crystals a yield criterion based on Schmid law is unsuitable due to the non-planar core of screw dislocations. Using atomic-scale information, Bassani et al. (2001); Vitek et al. (2004a,b) and Groger et al. (2008) formulated a yield criteria for BCC crystals that includes the effects of the non-Schmid components of stress tensor. Following their framework, a generalized resolved shear stress, τ^*_α, is defined in this work as a linear combination of the Schmid stress (τ^α) and other non-glide components of the stress tensor:

$$\tau^*_\alpha = \tau^\alpha + a_1\tau^\alpha_1 + a_2\tau^\alpha_2 + a_3\tau^\alpha_3 + a_4\tau^\alpha_4 + a_5\tau^\alpha_5, \tag{21}$$

where, τ^α_{1-5} are the non-glide stresses (Asaro and Rice, 1977) affecting the slip on system α by modifying the core of screw dislocations and a_{1-5} are material parameters that determine the relative importance of the different non-glide stresses. The set of the non-glide stresses τ^α_{1-5} introduced in the above equations are defined as

$$\begin{aligned}
\tau^\alpha_1 &= \boldsymbol{\tau} : (\boldsymbol{s}^{*(\alpha)} \otimes \boldsymbol{n}^{*(\alpha)}_1) = \boldsymbol{\tau} : \boldsymbol{\mu}^\alpha_1, \\
\tau^\alpha_2 &= \boldsymbol{\tau} : (\boldsymbol{s}^{*(\alpha)} \otimes \boldsymbol{n}^{*(\alpha)}_2) = \boldsymbol{\tau} : \boldsymbol{\mu}^\alpha_2, \\
\tau^\alpha_3 &= \boldsymbol{\tau} : ((\boldsymbol{s}^{*(\alpha)} \times \boldsymbol{m}^{*(\alpha)}) \otimes \boldsymbol{m}^{*(\alpha)}) = \boldsymbol{\tau} : \boldsymbol{\mu}^\alpha_3, \\
\tau^\alpha_4 &= \boldsymbol{\tau} : ((\boldsymbol{n}^{*(\alpha)}_1 \times \boldsymbol{s}^{*(\alpha)}) \otimes \boldsymbol{n}^{*(\alpha)}_1) = \boldsymbol{\tau} : \boldsymbol{\mu}^\alpha_4, \\
\tau^\alpha_5 &= \boldsymbol{\tau} : ((\boldsymbol{n}^{*(\alpha)}_2 \times \boldsymbol{s}^{*(\alpha)}) \otimes \boldsymbol{n}^{*(\alpha)}_2) = \boldsymbol{\tau} : \boldsymbol{\mu}^\alpha_5.
\end{aligned} \tag{22}$$

Here, $\boldsymbol{\tau}$ is the Kirchhoff stress and $\boldsymbol{n}^{*(\alpha)}_1 = \boldsymbol{F}^{*^{-T}}\boldsymbol{n}^{(\alpha)}_1$ and $\boldsymbol{n}^{*(\alpha)}_2 = \boldsymbol{F}^{*^{-T}}\boldsymbol{n}^{(\alpha)}_2$ are normals to non-glide planes for slip system α in the current configuration. The corresponding lattice vectors, $\boldsymbol{n}^{(\alpha)}_1$ and $\boldsymbol{n}^{(\alpha)}_2$, in reference configuration are listed in Table 1 for systems involving slip on $\{110\}$. Note, $\tau^\alpha, \tau^\alpha_1$ and τ^α_2 are parallel to the Burgers vector and τ^α_3, τ^α_4 and τ^α_5 are perpendicular to the Burgers vector.

We now redefine the effective resolved shear stress τ^α_{eff} by modifying its definition in Equations 18 to be

$$\tau^\alpha_{eff} = |\tau^*_\alpha| - g^\alpha = |\tau^\alpha + a_1\tau^\alpha_1 + a_2\tau^\alpha_2 + a_3\tau^\alpha_3 + a_4\tau^\alpha_4 + a_5\tau^\alpha_5| - g^\alpha \tag{23}$$

The macroscopically observed $\{112\}$ slip can be understood as a consequence of dislocations moving in a zig-zag fashion by elementary steps on the

ACCEPTED MANUSCRIPT

two most highly stressed $\{110\}$ planes of the same $\langle 111\rangle$ zone. Such pairs of $\{110\}$ slip systems (denoted as α_1 and α_2) for each $\{112\}$ slip are provided in Table 2. Therefore, non-glide shear stresses (τ^{α}_{1-5}) affecting the slip on $\{112\}$ systems are related to those non-glide shear stresses which affect the slip on their conjugate pair of $\{110\}$ slip systems. For example, slip on $(\bar{1}21)[\bar{1}\bar{1}1]$ ($\alpha = 21$ in Table 2) corresponds to equal slip on systems $(\bar{1}10)[\bar{1}\bar{1}1]$ and $(0\bar{1}\bar{1})[\bar{1}\bar{1}1]$ ($\alpha = 9$ and 7 in Table 1), and thus, the set of non-glide shear stresses for this slip system are obtained as $\tau^{21}_{1-5} = (\tau^{9}_{1-5} - \tau^{7}_{1-5})/\sqrt{3}$. The negative sign in the expression accounts for the slip direction of the second system in the pair.

2.2.3. Athermal slip resistance and hardening model

Since g^{α} represents the flow stress for slip system α, its evolution governs the hardening of the crystal. The rate of change of g^{α} is postulated as (Peirce et al., 1983)

$$\dot{g}^{\alpha} = \sum_{\beta=1}^{n} h_{\alpha\beta}|\dot{\gamma}^{\beta}|, \tag{24}$$

$$h_{\alpha\beta} = h_{\alpha} q_{\alpha\beta} \quad \text{No sum}, \tag{25}$$

$$h_{\alpha} = h_{\alpha/s} + (h_{\alpha/o} - h_{\alpha/s}) \ \operatorname{sech}^2\left(\frac{h_{\alpha/o} - h_{\alpha/s}}{g_{\alpha/s} - g_{\alpha/o}}\ \gamma^{\alpha}\right), \quad \text{and} \tag{26}$$

$$\gamma_t = \sum_{\alpha} |\ \gamma^{\alpha}|. \tag{27}$$

Here, $h_{\alpha\beta}$ are the latent hardening moduli which govern the interaction between various slip systems, and $\dot{\gamma}^{\beta}$ is the slip rate on the system β. The $h_{\alpha/\circ}$ and $h_{\alpha/s}$ are an initial and saturation hardening rate, and $g_{\alpha/\circ}$ and $g_{\alpha/s}$ are an initial and saturation yield stress, respectively, corresponding to the αth slip system. The γ_t is the sum of the plastic shear strains in all the slip systems. Note that, Equation (26) uses shear strain on individual slip systems, γ^{α} (Bassani and Wu, 1991). The $q_{\alpha\beta}$ in Equation (25) is the amplitude factor and govern the latent hardening behavior of crystal. (Lee et al., 1999) considered the types of possible dislocation junctions for the 24 slip systems in BCC crystals and provided the $q_{\alpha\beta}$ matrix (24×24) which is adopted in this work. This matrix is reproduced in Table 3 for the sake of completeness, keeping in mind the different slip system numbering used in this work. In this table, the letters O, N, C, G, W and S stand for self hardening, no junction, coplanar junction, glissile, weak sessile and strong sessile

Accepted manuscript

ACCEPTED MANUSCRIPT

junctions, respectively. The values of the above latent hardening coefficients are provided in Table 4.

2.3. Implementation of constitutive model

2.4. Rate-tangent formulation

The rate-tangent modulus scheme for implementing the above constitutive equations in a finite element code, discussed in detail by (Peirce et al., 1983), is presented in this section. First, an estimate is made of the change in shear rate, $\dot{\gamma}^{\alpha}$, during the current time increment and then an elastic-plastic forward gradient modulus is derived relating the increments of stress to those of strain.

Recall that the plastic slip rate is given by the Equations 18 and 20. The increment in plastic slip on a slip system α during the current time increment is defined as

$$\Delta\gamma^{\alpha} = \gamma^{\alpha}(t + \Delta t) - \gamma^{\alpha}(t). \tag{28}$$

A linear interpolation within the time increment is employed so that :

$$\Delta\gamma^{\alpha} = [(1-\theta)\dot{\gamma^{\alpha}}(t) + \theta\dot{\gamma^{\alpha}}(t + \Delta t)]\Delta t. \tag{29}$$

The parameter θ can range from 0 to 1, with $\theta = 0$ corresponding to the simple forward Euler time integration scheme, while, $\theta = 1$ represents backward integration. In the present work, θ is taken to be 0.5. Now a Taylor series (only first order terms) is used to approximate $\dot{\gamma^{\alpha}}(t + \Delta t)$ so that

$$\dot{\gamma^{\alpha}}(t + \Delta t) = \dot{\gamma^{\alpha}}(t) + \left.\frac{\partial\dot{\gamma^{\alpha}}}{\partial\tau^{\alpha}_{eff}}\right|_{t} \Delta\tau^{\alpha}_{eff} + \left.\frac{\partial\dot{\gamma^{\alpha}}}{\partial T}\right|_{t} \Delta T. \tag{30}$$

Here, a subscript after a vertical bar is used to denote the time at which the corresponding term is evaluated. From Equations 18 and 20, one can write

$$\left.\frac{\partial\dot{\gamma^{\alpha}}}{\partial\tau^{\alpha}_{eff}}\right|_{t} = \mathcal{A}^{\alpha}\left(\frac{\dot{\gamma^{\alpha}}(t)}{\tau_{\circ}}\right) \tag{31}$$

where,

$$\mathcal{A}^{\alpha} = \left(\frac{\Delta G_{k\circ}}{\kappa T}\right)(pq)\left[1 - \left(\frac{\tau^{\alpha}_{eff}}{\tau_{\circ}}\right)^{p}\right]^{q-1}\left(\frac{\tau^{\alpha}_{eff}}{\tau_{\circ}}\right)^{p-1} \tag{32}$$

Accepted manuscript

ACCEPTED MANUSCRIPT

and,

$$\left.\frac{\partial \dot{\gamma^{\alpha}}}{\partial T}\right|_{t} = \left(\frac{\Delta G_{k\circ}}{\kappa T}\right)\left(\frac{\dot{\gamma^{\alpha}}(t)}{T}\right). \tag{33}$$

Relations for $\Delta\tau^{\alpha}_{eff}$ are derived form Equation (23) as

$$\Delta\tau^{\alpha}_{eff} = |\Delta\tau^{\alpha} + a_1\Delta\tau^{\alpha}_1 + a_2\Delta\tau^{\alpha}_2 + a_3\Delta\tau^{\alpha}_3 + a_4\Delta\tau^{\alpha}_4 + a_5\Delta\tau^{\alpha}_5| - \Delta g^{\alpha} \tag{34}$$

With the help of Equation (2), the derivative of Equation (15) can be written as

$$\dot{\tau^{\alpha}} = \boldsymbol{s}^{*(\alpha)} \cdot (\overset{\nabla}{\boldsymbol{\tau}}{}^{*} + \boldsymbol{D}^{*}\boldsymbol{\tau} - \boldsymbol{\tau}\boldsymbol{D}^{*})\boldsymbol{m}^{*(\alpha)}. \tag{35}$$

By using Equations (8)-(10) one obtains,

$$\Delta\tau^{\alpha} = (\boldsymbol{L} : \boldsymbol{\mu}^{\alpha} + \boldsymbol{\beta}^{\alpha}) : \boldsymbol{D}^{*}\Delta t \tag{36}$$

Similarly, from Equation (22) one can derive

$$\begin{aligned}
\Delta\tau^{\alpha}_1 &= (\boldsymbol{L} : \boldsymbol{\mu}^{\alpha}_1 + \boldsymbol{\beta}^{\alpha}) : \boldsymbol{D}^{*}\Delta t \\
\Delta\tau^{\alpha}_2 &= (\boldsymbol{L} : \boldsymbol{\mu}^{\alpha}_2 + \boldsymbol{\beta}^{\alpha}) : \boldsymbol{D}^{*}\Delta t \\
\Delta\tau^{\alpha}_3 &= (\boldsymbol{L} : \boldsymbol{\mu}^{\alpha}_3 + \boldsymbol{\beta}^{\alpha}) : \boldsymbol{D}^{*}\Delta t \\
\Delta\tau^{\alpha}_4 &= (\boldsymbol{L} : \boldsymbol{\mu}^{\alpha}_4 + \boldsymbol{\beta}^{\alpha}) : \boldsymbol{D}^{*}\Delta t \\
\Delta\tau^{\alpha}_5 &= (\boldsymbol{L} : \boldsymbol{\mu}^{\alpha}_5 + \boldsymbol{\beta}^{\alpha}) : \boldsymbol{D}^{*}\Delta t
\end{aligned} \tag{37}$$

where $\boldsymbol{\mu}^{\alpha}_{1-5}$ follows from Equation (22). From Equation (24) one can write,

$$\Delta g^{\alpha} = \sum_{\beta=1}^{n} h_{\alpha\beta}|\Delta\gamma^{\beta}| \ . \tag{38}$$

Substitution of Equations (36)-(38) into Equation (34) leads to

$$\begin{aligned}
\Delta\tau^{\alpha}_{eff} &= |(\boldsymbol{R}^{\alpha}_{eff} : \boldsymbol{D}^{*}\Delta t)| - \sum_{\beta=1}^{n} h_{\alpha\beta}|\Delta\gamma^{\beta}| \\
&= \left|\boldsymbol{R}^{\alpha}_{eff} : \left(\boldsymbol{D}\Delta t - \sum_{\beta=1}^{n}\Delta\gamma^{\beta}\boldsymbol{\mu}^{\beta}\right)\right| - \sum_{\beta=1}^{n} h_{\alpha\beta}|\Delta\gamma^{\beta}|
\end{aligned} \tag{39}$$

Accepted manuscript

ACCEPTED MANUSCRIPT

where

$$\boldsymbol{R}^{\alpha}_{eff} = \big[\boldsymbol{L} : (\boldsymbol{\mu}^{\alpha} + a_1\boldsymbol{\mu}^{\alpha}_1 + a_2\boldsymbol{\mu}^{\alpha}_2 + a_3\boldsymbol{\mu}^{\alpha}_3 + a_4\boldsymbol{\mu}^{\alpha}_4 + a_5\boldsymbol{\mu}^{\alpha}_5) + (1 + a_1 + a_2 + a_3 + a_4 + a_5)\boldsymbol{\beta}^{\alpha}\big]. \tag{40}$$

On substituting Equations (31), (33) and (39) in Equation (30) and simplifying, one obtains:

$$\Delta\gamma^{\alpha} = \dot{f}^{\alpha}\Delta t + \boldsymbol{F^{\alpha}} : \boldsymbol{\Delta\epsilon} + \dot{\mathfrak{I}}^{\alpha}\Delta t \tag{41}$$

where,

$$\begin{aligned} \dot{f}^{\alpha} &= \sum_{\beta=1}^{n} M_{\alpha\beta}\dot{\gamma}^{\beta}(t), \\ \boldsymbol{F^{\alpha}} &= \sum_{\beta=1}^{n} M_{\alpha\beta}\boldsymbol{Q^{\beta}}, \\ \boldsymbol{\Delta\epsilon} &= \boldsymbol{D}\Delta t. \\ M_{\alpha\beta} &= N^{-1}_{\alpha\beta}, \\ N_{\alpha\beta} &= \delta_{\alpha\beta} + \frac{\theta\mathcal{A}^{\alpha}\dot{\gamma}^{\alpha}(t)\Delta t}{\tau_{\circ}}\left[\boldsymbol{R}^{\alpha}_{eff} : \boldsymbol{\mu}^{\beta} + h_{\alpha\beta}\right], \\ \boldsymbol{Q}^{\alpha} &= \frac{\theta\mathcal{A}^{\alpha}\dot{\gamma}^{\alpha}(t)\Delta t}{\tau_{\circ}}\boldsymbol{R}^{\alpha}_{eff}, \end{aligned} \tag{42}$$

and

$$\dot{\mathfrak{I}}^{\alpha} = \theta\left(\frac{\Delta G_{k\circ}}{\kappa T}\right)\left(\frac{\Delta T}{T}\right)\dot{\gamma}^{\alpha}(t) \tag{43}$$

Finally, Equation (41) allows the constitutive law Equation (14) to be written as

$$\overset{\nabla}{\boldsymbol{\tau}} = \boldsymbol{C} : \boldsymbol{D} - \dot{\boldsymbol{\chi}}. \tag{44}$$

Here, $\boldsymbol{C}$ is the elastic-plastic rate tangent modulus given by

$$\boldsymbol{C} = \boldsymbol{L} - \sum_{\alpha=1}^{n} \boldsymbol{R^{\alpha}} \otimes \boldsymbol{F^{\alpha}}, \tag{45}$$

Accepted manuscript

ACCEPTED MANUSCRIPT

and

$$\dot{\boldsymbol{\chi}} \triangleq \sum_{\alpha=1}^{n} \boldsymbol{R}^{\boldsymbol{\alpha}}(\dot{f}^{\alpha} + \dot{\mathfrak{I}}^{\alpha}). \tag{46}$$

2.5. Stress update procedure

A summary of the stress update procedure is presented here. Given the following at an integration point within an element : $\boldsymbol{F}_n^e$, $\boldsymbol{F}_n^p$, $\Delta\boldsymbol{\epsilon} = \boldsymbol{D}\Delta t$, $\boldsymbol{\tau}_n$, g_n^{α}, $\boldsymbol{F}_{n+1}$ and time increment $\triangle t = t_{n+1} - t_n$, the update proceeds as follows.

1. Compute lattice vectors in deformed configuration
   $\boldsymbol{s}^{*(\alpha)} = \boldsymbol{F}_n^e \boldsymbol{s}^{(\alpha)}$,
   $\boldsymbol{m}^{*(\alpha)} = \boldsymbol{F}_n^{e^{-T}} \boldsymbol{m}^{(\alpha)}$,
   $\boldsymbol{n}_1^{*(\alpha)} = \boldsymbol{F}_n^{e^{-T}} \boldsymbol{n}_1^{(\alpha)}$,
   $\boldsymbol{n}_2^{*(\alpha)} = \boldsymbol{F}_n^{e^{-T}} \boldsymbol{n}_2^{(\alpha)}$,

2. Compute
   $\boldsymbol{\mu}^{(\alpha)} = \frac{1}{2}(\boldsymbol{s}^{*(\alpha)} \otimes \boldsymbol{m}^{*(\alpha)} + \boldsymbol{m}^{*(\alpha)} \otimes \boldsymbol{s}^{*(\alpha)})$,
   $\boldsymbol{\omega}^{(\alpha)} = \frac{1}{2}(\boldsymbol{s}^{*(\alpha)} \otimes \boldsymbol{m}^{*(\alpha)} - \boldsymbol{m}^{*(\alpha)} \otimes \boldsymbol{s}^{*(\alpha)})$,
   $\boldsymbol{\beta}^{\boldsymbol{\alpha}} = \boldsymbol{\omega}^{(\alpha)} \boldsymbol{\tau}_n - \boldsymbol{\tau}_n \boldsymbol{\omega}^{(\alpha)}$,
   $\boldsymbol{R}^{\boldsymbol{\alpha}} = \boldsymbol{L} : \boldsymbol{\mu}^{(\alpha)} + \boldsymbol{\beta}^{\boldsymbol{\alpha}}$,
   Schmid stress : $\tau^{(\alpha)} = \boldsymbol{\tau}_n : \boldsymbol{\mu}^{\alpha}$.

3. Compute
   $\boldsymbol{\mu}_1^{\alpha} = (\boldsymbol{s}^{*(\alpha)} \otimes \boldsymbol{n}_1^{*(\alpha)})$
   $\boldsymbol{\mu}_2^{\alpha} = (\boldsymbol{s}^{*(\alpha)} \otimes \boldsymbol{n}_2^{*(\alpha)})$
   $\boldsymbol{\mu}_3^{\alpha} = ((\boldsymbol{s}^{*(\alpha)} \times \boldsymbol{m}^{*(\alpha)}) \otimes \boldsymbol{m}^{*(\alpha)})$
   $\boldsymbol{\mu}_4^{\alpha} = ((\boldsymbol{n}_1^{*(\alpha)} \times \boldsymbol{s}^{*(\alpha)}) \otimes \boldsymbol{n}_1^{*(\alpha)})$
   $\boldsymbol{\mu}_5^{\alpha} = ((\boldsymbol{n}_2^{*(\alpha)} \times \boldsymbol{s}^{*(\alpha)}) \otimes \boldsymbol{n}_2^{*(\alpha)})$
   $\boldsymbol{R}_{eff}^{\alpha}$ from Equation (40)
   Non-Schmid stresses : $\tau_{1-5}^{(\alpha)} = \boldsymbol{\tau}_n : \boldsymbol{\mu}_{1-5}^{\alpha}$

4. Compute
   $\tau_{eff}^{\alpha} = |\tau^{\alpha} + a_1\tau_1^{\alpha} + a_2\tau_2^{\alpha} + a_3\tau_3^{\alpha} + a_4\tau_4^{\alpha} + a_5\tau_5^{\alpha}| - g^{\alpha}$

5. Check effective resolved shear stress :
   If $\tau_{eff}^{\alpha} \leq 0$, then perform an elastic step. Otherwise, perform plastic

Accepted manuscript

ACCEPTED MANUSCRIPT

steps 6-8

6. Compute ΔG_k^α from Equation (20) and then $\dot{\gamma}^\alpha$ from Equation (18). Also, compute $\dot{f}^\alpha, \boldsymbol{F}^{\boldsymbol{\alpha}}, \boldsymbol{Q}^{\boldsymbol{\alpha}}, \dot{\mathfrak{J}}^\alpha$, and $N_{\alpha\beta}$ from eq(42). Invert $N_{\alpha\beta}$. Hence compute $\Delta\gamma_{n+1}^\alpha$ from Equation (41).

7. Update $\boldsymbol{F}_{n+1}^p$; $\boldsymbol{F}_{n+1}^e$; $\boldsymbol{\tau}_{n+1}$ and slip resistance g_{n+1}^α as follows:
$\boldsymbol{L}^p = \sum_{\alpha=1}^n \dot{\gamma}^\alpha(\boldsymbol{s}^{*(\alpha)} \otimes \boldsymbol{m}^{*(\alpha)})$,
$\boldsymbol{F}_{n+1}^p = \boldsymbol{F}_n^p + \boldsymbol{L}^p * \boldsymbol{F}_n^p$,
$\boldsymbol{F}_{n+1}^e = \boldsymbol{F}_{n+1} * \boldsymbol{F}_{n+1}^{p^{-1}}$,
$\boldsymbol{\tau}_{n+1} = \boldsymbol{\tau}_n + (\boldsymbol{L} : \Delta\boldsymbol{\epsilon} - \sum_{\alpha=1}^n \boldsymbol{R}^{\boldsymbol{\alpha}} \Delta\gamma_{n+1}^\alpha)$ and
$g_{n+1}^\alpha = g_n^\alpha + \sum_{\beta=1}^n h_{\alpha\beta}^n |\dot{\gamma}_{n+1}^\beta|$.

8. Compute the elastic-plastic rate tangent modulus:
$\boldsymbol{C} = \boldsymbol{L} - \sum_{\alpha=1}^n \boldsymbol{R}^{\boldsymbol{\alpha}} \otimes \boldsymbol{F}^{\boldsymbol{\alpha}}$.
$\dot{\boldsymbol{\chi}} = \sum_{\alpha=1}^n \boldsymbol{R}^{\boldsymbol{\alpha}}(\dot{f}^\alpha + \dot{\mathfrak{J}}^\alpha)$.

3. Finite element formulation for incremental static equilibrium

In the present work, an updated Lagrangian procedure is employed, which is quite convenient from the point of view of computer implementation. To this end, a reference configuration is chosen, which coincides instantaneously with the current configuration. The variational principle written in terms of the Kirchoff stress and its Jaumann rate referred to the current configuration is given by (refer McMeeking and Rice, 1975):

$$\int_{V_t} \left[\overset{\nabla}{\boldsymbol{\tau}}_{ij} - (\tau_{ik}D_{kj} + D_{ik}\tau_{kj})\right] \delta D_{ij} dV + \int_{V_t} \tau_{ij} v_{k,j} \delta v_{k,i} dV = \int_{V_t} \dot{b}_j \delta v_j dV + \int_{S_T} \dot{T}_j \delta v_j dA, \tag{47}$$

where all integrations are performed over the current volume V_t and the boundary segment S_T in the equilibrium configuration corresponding to time t. In the above equation, $D_{ij} = (\partial v_i/\partial x_j + \partial v_j/\partial x_i)/2$, denotes the rate of deformation tensor and $v_{k,i} = l_{ki} = \partial v_k/\partial \mathrm{x}_i$ is the spatial gradient of particle velocity vector. Further, $\dot{b}_j$ and $\dot{T}_j$ represent nominal body force and surface traction rates based on the current volume and surface area. It will be assumed here that $\dot{\boldsymbol{b}}$ and $\dot{\boldsymbol{T}}$ are fully prescribed.

Accepted manuscript

ACCEPTED MANUSCRIPT

The sum of the second and third terms in the first integral in the left hand side of Equation (47) can be expressed as follows:

$$\tau_{ik}D_{kj} + D_{ik}\tau_{kj} = \hat{L}_{ijkl}D_{kl}, \tag{48}$$

where the tensor $\hat{L}_{ijkl}$ is given by,

$$\hat{L}_{ijkl} = \frac{1}{2}(\tau_{ik}\delta_{lj} + \tau_{il}\delta_{kj} + \tau_{kj}\delta_{il} + \tau_{lj}\delta_{ik}). \tag{49}$$

Note that the tensor $\hat{L}_{ijkl}$ satisfies all the major and minor symmetries. Using Equations (44), (48) and (49) into variational principle (47), one obtains:

$$\begin{aligned}\int_{V_t} \delta D_{ij}C_{ijkl}D_{kl}dV \quad &- \quad \int_{V_t} \delta D_{ij}\hat{L}_{ijkl}D_{kl}dV + \int_{V_t} \tau_{ij}v_{k,j}\delta v_{k,i}dV \\ &= \quad \int_{V_t} \dot{\chi}_{ij}\delta D_{ij}dV + \int_{V_t} \dot{b}_j\delta v_j dV + \int_{S_T} \dot{T}_j\delta v_j dA\end{aligned} \tag{50}$$

At this point, the finite element approximation is introduced as $\{v\} = [N]\{\dot{U}\}$, where $[N]$ is the matrix of shape functions and $\{\dot{U}\}$ is the vector of nodal point velocities. Then spacial gradient of velocity can be expressed in terms of the nodal point velocities as $\{D\} = [B]\{\dot{U}\}$, where $[B]$ is the spatial gradient of the shape function matrix. The finite element equations for rate equilibrium can be derived from Equation (50) following the usual finite element procedure (see Bathe, 1996) as:

$$[K]^e\{\dot{U}\} = \{\dot{F}_\chi\} + \{\dot{F}_b\} + \{\dot{F}_t\}. \tag{51}$$

The element stiffness matrix $[K]^e$ is comprised of three parts as:

$$[K]^e = [K^{(1)}]^e - [K^{(2)}]^e + [K^{(3)}]^e. \tag{52}$$

Here,

$$[K^{(1)}]^e = \int_{V_t^e} [B]^T[C][B]dV^e \tag{53}$$

is the tangent stiffness matrix arising from material nonlinearity. The matrix $[C]$ contains the terms of the elastic-plastic constitutive tensor C_{ijkl} (see, Equation (45)). Since C_{ijkl} satisfy major symmetry, the matrix $[C]$ and hence $[K^{(1)}]^e$ are symmetric.

Accepted manuscript

ACCEPTED MANUSCRIPT

The second and third matrices in the right hand side of Equation (52) comprise the initial stress stiffness. The matrix $[K^{(2)}]^e$ is given by,

$$[K^{(2)}]^e = \int_{V_t^e} [B]^T [\hat{L}][B] dV^e, \tag{54}$$

where the matrix $[\hat{L}]$ contains the terms of $\hat{L}_{ijkl}$. It can be shown that the terms of the stiffness matrix $[K^{(3)}]^e$ are given by:

$$K^{(3)}_{iajb} = \int_{V_t^e} B^a_l \tau_{lk} B^b_k \delta_{ij} dV^e, \tag{55}$$

where $(i, j) \in [1, 3]$ and $(a, b) \in [1, n_e]$ with $n_e =$ number of nodes per element. The element force rate vectors $\{\dot{F}_\chi\}$, $\{\dot{F}_b\}$ and $\{\dot{F}_t\}$ are defined as follows:

$$\{\dot{F}_\chi\}^e = \int_{V_t^e} [B]^T \{\dot{\chi}\} dV^e, \tag{56}$$

$$\{\dot{F}_b\}^e = \int_{V_t^e} [N]^T \{\dot{b}\} dV^e \tag{57}$$

and

$$\{\dot{F}_t\}^e = \int_{S_T^e} [N]^T \{\dot{T}\} dV^e. \tag{58}$$

Here, $\{\dot{F}_\chi\}$ is the nodal rate vector force due to the $\dot{\chi}$ term in the variational principle (50), and $\{\dot{F}_b\}$, $\{\dot{F}_t\}$ are nodal force rate vectors due body force and surface tractions, respectively. These are represented here as column vectors.

The above finite element formulation has been implemented in the commercial finite element code ABAQUS (Simulia, 2009) by writing a user element sub-routine (UEL) for eight-noded isoparametric hexahedral elements. The finite element formulation is modified to treat the nearly incompressible deformation using $\bar{\text{B}}$-formulation (Moran et al., 1990).

4. Material parameters for molybdenum crystal

As a representative of BCC transition metals, molybdenum is a suitable candidate to apply the constitutive model presented in this paper. The material constants in the model are determined by calibrating the model against existing experimental data on Mo single crystal. A systematic two-step pro-

Accepted manuscript

ACCEPTED MANUSCRIPT

cedure is provided for determination of these material constants without compromising their physical interpretation. In the first step, the material properties of this BCC crystal which govern the temperature dependence of yield stress are determined. Then the remaining properties are determined in the second step to capture the orientation dependence of yielding and hardening behavior.

The three stiffness parameters (C_{11}, C_{12} and C_{44}) that characterize the anisotropic elasticity tensor of Mo crystals are provided by (Bolef and Klerk, 1998), as a function of temperature. However, in order to simplify the analysis and interpretation of results, the temperature dependence of the stiffness parameters is ignored in this work. Note that the temperature dependence of the elastic moduli of molybdenum is negligibly small compared with the steep increase of the flow stress with decreasing temperature. The three stiffness parameters of Mo are given in Table 5.

Recall the expression for the plastic slip rate given by Equation (18). Experimental observations suggest that for BCC metals, the activation enthalpy ΔG_k is proportional to the temperature over a wide range at a given strain rate. In other words, $\Delta G_k/\kappa T \approx C$, where, C is a constant, and is about 23–27 for BCC transition metals. Experimentally, C is found to be about 24 for tantalum (Argon and Maloof, 1977) and about 25 for tungsten (Brunner and Glebovsky, 2000) and molybdenum (Hollang et al., 1997). Therefore, assuming $\Delta G_k/\kappa T = 25$ and with the help of Equations (20) and (23) one can write

$$\tau_\alpha^* = g_o^\alpha + \tau_\circ \left[1 - \left(\frac{25\kappa T}{\Delta G_{k\circ}}\right)^{\frac{1}{q}}\right]^{\frac{1}{p}}. \tag{59}$$

Equation (59) defines the generalized resolved stress τ_α^* as a function of temperature and can be used to fit the experimentally observed dependence of critical resolved shear stress (CRSS) on temperature. It is emphasized that g_0^α is the athermal part of the critical resolved shear stress due to long range barriers and is assumed to be constant over the entire temperature range. Effectively this is the resistance offered by crystals to the plastic deformation at high temperatures when thermal activation annuls the short range barriers, like lattice resistance. In contrast, $\tau_\circ$ is usually interpreted as the critical resolved shear stress required to initiate the plastic flow when the temperature approaches absolute zero and thermal activation plays no significant role.

The critical resolved shear stress for Mo single crystal as a function of

Accepted manuscript

ACCEPTED MANUSCRIPT

temperature was compiled by (Kaufmann et al., 1984), and is reproduced in Figure 3. From Figure 3, we use following estimates: $g_0^\alpha = 2$ MPa and $\tau_\circ = 665$ MPa. Using these values, the remaining parameters in Equation (59) are determined by fitting the experimental data as shown in Figure 3. The fitting procedure yields $\Delta G_{k\circ} = 0.16568$E-18 J (or 1.03 eV), $p = 0.5$ and $q = 1.25$ (see Table 6). These properties are assumed to be identical for all the slip systems. A similar procedure was used by Tang et al. (1998) previously in the case of tantalum, which experiences a similar thermally activated motion of screw dislocations.

In the remaining set of material properties, the quantities a_1–a_5 in Equation (21) are initially assumed to be identical for all the slip systems, whereas, the quantities $h_\circ, h_s, g_\circ$ and g_s in the hardening Equation (26) are taken to be different for different groups of slip systems, based on whether slip occurs in twin sense or anti-twin sense. These material parameters are determined by calibrating the model against existing experimental results on pure molybdenum single crystals. The experimental stress-strain curves shown in Figure 4 and Figure 5 are taken from Irwin et al. (1974) and Kaufmann et al. (1984), and are reproduced in Figure 4. These experimental stress-strain curves were obtained from uniaxial tension tests carried out at 293 K, with a strain rate of 6.0E-5 s^{-1} and for three different orientations, namely [010], [111] and [101], along the tensile loading axis. It can be seen from Figure 4 that the orientation of the crystal strongly influences its yielding and hardening behavior. The rate of strain hardening is relatively high at initial stages of deformation but saturates rapidly as deformation progresses. (Irwin et al., 1974) report results for loading in tension and loading in compression along aforementioned orientations. We use experimental data from (Irwin et al., 1974) to calibrate the orientation dependence of stress-strain response. In addition, (Guiu and Pratt, 1966) reported experimental results on the temperature dependence of stress-strain response in tension along [101], and we will use this data to validate temperature dependence from our simulated results for molybdenum.

The simulations were performed using the finite element formulation discussed in Sec. 3, and using a single hexahedral element with loading and temperature conditions similar to those used in the above experiments. All the remaining material parameters in the model are then determined by laborious optimization to get tensile stress-strain curves from the simulations that are representative of those observed in the experiments for different crystal orientations (see Figure 4). The complete list of material parameters

Accepted manuscript

ACCEPTED MANUSCRIPT

hence determined using this two-step procedure for molybdenum crystals is provided in Tables 7 and 8.

It is imperative to check if the material properties determined so far can indeed predict the yielding and hardening behavior of molybdenum crystals at different temperatures. To this end, a direct comparison of experimental observations with 3D finite element predictions of the resolved shear stress versus strain response at various temperatures (with [110] as the tensile axis) are presented in Figure 5. The experimental results are taken from Kaufmann et al. (1984), Kopetskii and Pashkovskii (1974), Guiu and Pratt (1966) and Irwin et al. (1974). The specific temperatures considered are 293 K, 353 K, 423 K and 573 K. Figure 5 shows that the finite element simulation predictions are in reasonable agreement with the experimental observation.

Now, to understand the dependence of flow stress on rate of deformation, recall again Equations (18) and (20) for the plastic slip rate. One can write from these equations:

$$\frac{\tau^{\alpha}_{eff}}{\tau_{\circ}} = \left\{ 1 - \left[\ln\left(\frac{\dot{\gamma}^{\alpha}_{\circ}}{\dot{\gamma}^{\alpha}} \right) \frac{\kappa T}{\Delta G_{k\circ}} \right]^{\frac{1}{q}} \right\}^{\frac{1}{p}} . \tag{60}$$

This expression is plotted in Figure 6, after substituting the material properties of Mo determined earlier. Figure 6 exemplifies the dependence of the effective resolved stress ($\tau^{\alpha}_{eff}/\tau_{\circ}$) on temperature for various strain rates ($\dot{\gamma}^{\alpha}/\dot{\gamma}^{\alpha}_{\circ}$). It can be observed that as the temperature increases, the τ^{α}_{eff} required to initiate the plastic flow decreases and approaches zero at the critical temperature when thermal activation is sufficient to overcome the lattice friction. This critical temperature increases with increasing rate of deformation. Therefore, the model suggests (as is to be expected with a thermally activated approach) that the effect of increasing strain rate is analogous to decreasing the temperature and vice-versa. Note that at very high strain rates ($\dot{\gamma}^{\alpha} > 10^6 s^{-1}$), plasticity may be controlled by viscous drag experienced by rapidly moving dislocations. Such effects are not considered in this work.

5. Evaluation of the model: Compression of a single crystal with a through-hole

An assessment was made of the ability of the calibrated model to predict localized heterogeneous deformation in a specimen with a hole. First,

Accepted manuscript

ACCEPTED MANUSCRIPT

the calibration of material parameters (in the earlier section) was performed using a single finite element, and was based solely on the comparison of stress-strain data assuming conditions of homogeneous deformation. Following this, within the simulation framework, solutions were obtained for non-uniform stress field resulting from heterogeneities in the specimen or complex boundary conditions. Corroboration of computed deformation fields with experimental measures of the deformations can then provide an assessment of the calibrated model.

For this evaluation, we consider the non-uniform deformation resulting from the macroscopic compression of a Mo single crystal containing a cylindrical hole. Such an experiment can provide controlled heterogeneous deformation field in the vicinity of the hole. In the case of an isotropic linear elastic material, the solution of the resulting deformation field is well-known from elasticity. However, in the case of a single crystal specimen undergoing large deformation, simulations incorporating the calibrated model are required to predict the heterogeneous nature of plastic deformation.

Single-crystal Mo with 99.999% (3N) purity obtained from the Metal Crystals (U.K.) was used for the experiment. The crystallographic orientation was confirmed using back reflection Laue diffraction. Mis-orientations of less than 1° were observed, which are within acceptable limits. Figure 7 is a schematic showing the specimen geometry, orientation and loading conditions. A rectangular specimen (8 mm x 4 mm x 2.5 mm in dimension) was machined, and, a cylindrical hole with a diameter of 0.4 mm was made at the center of the plate using electro discharge machining (EDM). Electron back scattered diffraction (EBSD) performed on the as-machined sample indicated that no significant lattice rotations were induced due to machining. The two sides of the sample were polished using standard metallographic polishing methods to a surface roughness of 0.5 µm. Samples for EBSD were prepared by a two step procedure. First, they were polished using colloidal silica with 50 nm particles for about 120 min, followed by polishing with distilled water for 5 min.

Uniaxial compression experiments were carried out using an MTS servo hydraulic machine under displacement controlled mode and at a nominal strain rate of $10^{-3}\ s^{-1}$. The specimen was compressed along the [001] axis of the single crystal. The two ends of the specimen that were in contact with the platen were lubricated to minimize friction during compression. The macroscopic compressive stress-strain curve of a specimen deformed to a maximum strain of 0.06 is calculated from the instrumented load-displacement data

Accepted manuscript

ACCEPTED MANUSCRIPT

and initial dimensions of the specimen.

Post-deformation characterization of the specimen was carried out using optical imaging, scanning electron microscopy (SEM) and a laser profilometer. For the SEM imaging, the (110) surface (in the plane of the hole) was polished to aid visualization of strain-localized bands. Measurements from the laser profilometer assist in quantitative comparison of out-of-plane displacements around the hole. Microscopic characterization was also performed using Electron Backscattered Diffraction (EBSD). The EBSD images indicate that there are no significant lattice rotations as a result of EDM and the inverse pole figure (IPF) map further confirms the (110) orientation of the crystal. The SEM images indicate that the initial shape of the hole is relatively cylindrical, although there are small machining artifacts, particularly at the periphery of the hole.

5.1. Comparison of predictions with experimental measurements

Simulations of Mo undergoing compression are performed by applying finite-displacement boundary condition (positive Y-face, which is also crystallographic plane (001) in Figure 7) under a constant nominal strain rate. Finite element computed reaction forces at the nodes of positive (001) face are used to calculate nominal stress σ_{yy}.

The macroscopic stress-strain curve obtained from crystal plasticity simulations for this specimen geometry is plotted in Figure 8 for comparison with results from the experiment. The two curves are in excellent agreement after 2% strain. The experimentally obtained behavior is much more compliant during early stages of deformation, due to the combined influences of machine compliance, measurement resolution and imperfect specimen geometry. At 2% strain, for the sample dimensions used in the present study, the resolution of the linear variable displacement transducer (LVDT) sensor was insufficient making the displacement and thus average strain measurement not accurate during small deformations. The experiments are thus not able to provide an accurate specimen stiffness at small strains. The onset of local yield is also not captured by the simulations, perhaps also because of differences in purity between the crystal at hand and those used to obtain the calibration data.

The overall dimensions of deformed specimens were quantitatively compared. From the simulation, for 6.00% engineering strain along Y (loading direction), the lateral expansion along X direction was 3.96%. From the experiment, for 5.37% engineering strain along Y direction, the lateral expan-

Accepted manuscript

ACCEPTED MANUSCRIPT

sion along X direction was 2.61%. Re-examining the experimental method, the friction at the compression platens may alter (due to lateral constraint) overall deformation of the specimen and thus shape of the hole after deformation. On the other hand, the boundary condition in the simulations is frictionless at the top and bottom surfaces of the specimen, resulting in over-prediction of lateral expansion.

Figure 9 shows post-deformation images (at a macroscopic strain of 0.06) of the cylindrical hole obtained from experiments (top left insert) and simulations (bottom insert) respectively. Both the images indicate that the shape of the cylindrical hole changes into an elliptical cylinder. Slight differences in the length of the major and minor axes are observed between the experiments and simulations: the disagreement in measured lengths of major and minor axis from simulations, compared to experiments, is -16.5% and +9.0%, respectively. These differences could be due to the finite roughness of the cylindrical hole and scratches at the surface associated with machining, which are excluded from simulations. The regions (bands) that are visibly darker (compared to lighter grayscale material surrounding the hole) are predicted to have high out-of-place deformation, likely due to localized slip. Four such contiguous bands were visible, emanating from the elliptical hole. Each of these bands is (in theory) composed of slip traces. These slip traces make 40^0 to 43^0 with respect to the major axis of the elliptical hole on either side.

To further examine the strain localization near the hole, the sample was polished to observe the through-thickness character of these slip traces. Polishing may remove some traces from the sample, but was essential to obtain a flat surface for imaging. Figure 9 (top left insert) confirms the slip traces near the hole were not just on the specimen surface but also inside the specimen. These slip traces are indeed representative of localized deformation near the elliptical hole.

Figure 10 presents the laser profilometer images of the deformed sample providing the out plane displacements (represented by the color codes) around the elliptical hole as a result of deformation. It is observed that along the edges of the major axis of the ellipse, there is more out of plane displacement compared to the minor axis. The depth profiles (representing the relative height of the out of plane displacement with respect to the reference surface) are measured using a line scan and are presented in Figure 10. After deformation, the cylindrical hole became an elliptical hole, with minor and major axis measuring 0.314 mm $\times$ 0.428 mm from the experiment, and 0.262 mm $\times$ 0.466 mm from the simulation. While the simulation captures

Accepted manuscript

ACCEPTED MANUSCRIPT

the shape trends, some quantitative differences between experiment and simulation remain (as has been the case with most crystal plasticity models that examine heterogeneous plastic deformations).

In summary, this work addresses temperature, rate and orientation dependence of yield stress, including the dependence on non-Schmid effect, for crystal plasticity of BCC metals. The model was calibrated based on uniaxial experiments and was then used to satisfactorily predict localized deformation and flow stress response of molybdenum specimen with a hole.

6. Conclusions

A physics-based finite strain crystal plasticity constitutive model for body-centered-cubic (BCC) single crystals is developed to describe the strong temperature, rate and orientation dependence of the yield stress as well as twinning-anti-twinning asymmetry of shearing resistance. The flow rule is formulated based on the theory of thermally activated motion of screw dislocations via nucleation of double kinks. A yield criterion that incorporates atomistics-informed non-Schmid effects is used in the model. The material constants in the model are calibrated against existing experimental data on single-crystals of Molybdenum. The model can effectively describe the response of molybdenum single crystal up to homologous temperature of the order 0.3. Flow stress from simulations results on compression of a single crystal specimen with a hole had good agreement with experiment. In addition, the simulated localized deformation around the hole had qualitative agreement with experimentally characterized deformations.

Acknowledgments

This work was performed under the auspices of the Center for Advanced Metallic and Ceramic Systems at The Johns Hopkins University. The research was sponsored in part by the Army Research Laboratory (ARMAC-RTP) under the ARMAC-RTP Cooperative Agreement Number DAAD19-01-2-0003. Some support of NPD and KTR also came from ARL under Cooperative Agreement Number W911NF-12-2-0022, and this is deeply appreciated.

Accepted manuscript

ACCEPTED MANUSCRIPT

Data availability

The raw data required to reproduce these findings are available to download from nitin@jhu.edu. The processed data required to reproduce these findings are available to download from nitin@jhu.edu.

References

Taylor, G.. Thermally activated deformation of bcc metals and alloys. Progress in Materials Science 1992;:29–61.

Ito, K., Vitek, V.. Atomistic study of non-Schmid effects in the plastic yielding of bcc metals. Philosophical Magazine 2001;81:1387–1407.

Vitek, V.. Computer simulation of the screw dislocation motion in b.c.c. metals under the effect of the external shear and uniaxial stresses. Proc R Soc Lond A 1976;352:109–124.

Woodward, C., Rao, S.I.. Ab-initio simulation of isolated screw dislocations mo and ta. Philosophical Magazine A 2001;81:1305–1316.

Kocks, U.F., Argon, A.S., Ashby, M.F.. Thermodynamics and Kinetics of Slip; vol. 19. Pergamon Press, Oxford; 1975.

Tang, M., Kubin, L.P., Canova, G.R.. Dislocation mobility and the mechanical response of BCC single crystals: a mesoscopic approach. Acta Materialia 1998;46:3221–3235.

Vitek, V., Mrovec, M., Bassani, J.L.. Influence of non glide stresses on plastic flow: from atomistic to continuum modeling. Material Science Engineering (A) 2004a;365:31–37.

Vitek, V., Mrovec, M., Groger, R., Bassani, J.L., Racherla, V., Yin, L.. Effects of non-glide stresses on the plastic flow of single and polycrystals of molybdenum. Material Science Engineering (A) 2004b;387-389:138–142.

Taylor, G.I., Elam, C.F.. The distortion of iron crystals. Proc R Soc London A 1926;112:337–361.

Hollang, L., Hommel, M., Seeger, A.. The flow stress of ultra-high-purity molybdenum single crystals. Phys Stat Sol A 1997;160:329–354.

Accepted manuscript

ACCEPTED MANUSCRIPT

Seeger, A.. Why anomalous slip in body-centred cubic metals? Material Science Engineering (A) 2001;319-321:254–260.

Seeger, A.. Experimental evidence for the 110 to 112 transformation of the screw-dislocation cores in body-centred cubic metals. Phys Stat Sol A 2004;201:R21– R24.

Seeger, A., Wasserbach, W.. Anomalous slip - a feature of high-purity body-centred cubic metals. Phys Stat Sol A 2002;187:27–50.

Liao, K.C., Friedman, P.A., Pan, J.. Texture development and plastic anisotropy of b.c.c. strain hardening sheet metals. International Journal of Solids and Structures 1998;35:5205–523.

Lee, Y.J., Subhash, G., Ravichandran, G.. Constitutive modeling of textured body-centered-cubic (bcc) polycrystals. International Journal of Plasticity 1999;15:625–645.

Peirce, D., Asaro, R.J., Needleman, A.. Material rate dependence and localized deformation in crystalline solids. Acta Metall 1983;31:1951–1976.

Kothari, M., Anand, L.. Elasto-viscoplastic constitutive equations for polycrystalline metals: application to tantalum. Journal of the Mechanics and Physics of Solids 1998;46:51–83.

Xie, C.L., Ghosh, S., Groeber, M.. Modeling cyclic deformation of hsla steels using crystal plasticity. Journal of Engineering Materials and Technology 2004;126:339–352.

Ganapathysubramanian, S., Zabaras, N.. Modeling the thermoelastic-viscoplastic response of polycrystals using a continuum representation over the orientation space. International Journal of Plasticity 2005;21:119–144.

Yalcinkaya, T., Brekelmans, W.A.M., Geers, M.G.D.. BCC single crystal plasticity modeling and its experimental identification. Modelling and Simulation in Materials Science and Engineering 2008;16:085007.

Asaro, R.J.. Crystal plasticity. Journal of Applied Mechanics 1983;50:921–934.

Lawley, A., Gaigher, H.L.. Deformation structures in zone-melted molybdenum. Philosophical Magazine 1964;10:1478–6443.

Accepted manuscript

ACCEPTED MANUSCRIPT

Bassani, J.L., Ito, K., Vitek, V.. Complex macroscopic plastic flow arising from non-planar dislocation core structures. Material Science Engineering (A) 2001;319-321:97–101.

Groger, R., Racherla, V., Bassani, J.L., Vitek, V.. Multiscale modeling of plastic deformation of molybdenum and tungsten: Ii. yield criterion for single crystals based on atomistic studies of glide of 1/2[111] screw dislocations. Acta Materialia 2008;56:5412–5425.

Asaro, R.J., Rice, J.. Strain localization in ductile single crystals. Journal of the Mechanics and Physics of Solids 1977;25:309–338.

Bassani, J.L., Wu, T.Y.. Latent hardening in single crystals ii. analytical characterization and predictions. Proc R Soc Lond A 1991;435:21–41.

McMeeking, R.M., Rice, J.R.. Finite-element formulations for problems of large elastic-plastic deformation. International Journal of Solids and Structures 1975;11:601–616.

Bathe, K.J.. Finite Element Procedures. USA: PRH; 1996.

Simulia, . ABAQUS/Standard users manual version 6.9 EF. RI USA: Abaqus; 2009.

Moran, B., Ortiz, M., Shih, C.F.. Formulation of implicit finite element methods for multiplicative finite deformation plasticity. International Journal of Numerical methods in Engineering 1990;29:483–514.

Bolef, D.I., Klerk, J.D.. Elastic constants of single-crystal Mo and W between 77 and 500 k. Journal of Applied Physics 1998;33:2311–2314.

Argon, A.S., Maloof, S.R.. Slip in high purity tantalum between 0.7 and 40 k. Acta Metallurgica 1977;25:1485–1490.

Brunner, D., Glebovsky, V.. Analysis of flow-stress measurements of high-purity tungsten single crystals. Materials Letters 2000;44:144–152.

Kaufmann, H.J., Luft, A., Schulze, D.. Deformation mechanism and dislocation structure of high-purity molybdenum single crystals at low temperatures. Crystal Res & Technol 1984;19:357–372.

Accepted manuscript

ACCEPTED MANUSCRIPT

Irwin, G.J., Guiu, F., Pratt, P.L.. The influence of orientation on slip and strain hardening of molybdenum single crystals. Phys Stat Sol A 1974;22:685–698.

Guiu, F., Pratt, P.L.. The effect of orientation on the yielding and flow of molybdenum single crystals. Phys Stat Sol A 1966;15:539–552.

Kopetskii, C.V., Pashkovskii, A.I.. Plastic deformation and dislocation structure of molybdenum single crystals upon extending along [110] and [100] axes in the range from 77 to 573 k. Phys Stat Sol A 1974;21:741–751.

Accepted manuscript

ACCEPTED MANUSCRIPT

α	$\boldsymbol{m}^{(\alpha)}$	$\boldsymbol{s}^{(\alpha)}$	$\boldsymbol{n}_1$	$\boldsymbol{n}_2$
1	111	$01\bar{1}$	$\bar{1}10$	$10\bar{1}$
2	111	$\bar{1}01$	$0\bar{1}1$	$\bar{1}10$
3	111	$1\bar{1}0$	$10\bar{1}$	$0\bar{1}1$
4	$\bar{1}11$	$\bar{1}0\bar{1}$	$\bar{1}\bar{1}0$	$01\bar{1}$
5	$\bar{1}11$	$0\bar{1}1$	101	$\bar{1}\bar{1}0$
6	$\bar{1}11$	110	$01\bar{1}$	101
7	$\bar{1}\bar{1}1$	$0\bar{1}\bar{1}$	$1\bar{1}0$	$\bar{1}0\bar{1}$
8	$\bar{1}\bar{1}1$	101	011	$1\bar{1}0$
9	$\bar{1}\bar{1}1$	$\bar{1}10$	$\bar{1}0\bar{1}$	011
10	$1\bar{1}1$	$10\bar{1}$	110	$0\bar{1}\bar{1}$
11	$1\bar{1}1$	011	$\bar{1}01$	110
12	$1\bar{1}1$	$\bar{1}\bar{1}0$	$0\bar{1}\bar{1}$	$\bar{1}01$

Table 1: $\{110\}$ family of slip systems in BCC crystals and their corresponding non-glide planes. Note that the crystallographic vectors $\boldsymbol{m}^{(\alpha)}$, $\boldsymbol{s}^{(\alpha)}$, $\boldsymbol{n}_1$ and $\boldsymbol{n}_2$ have to be normalized before their use.

Accepted manuscript

ACCEPTED MANUSCRIPT

α	$\boldsymbol{m}^{(\alpha)}$	$\boldsymbol{s}^{(\alpha)}$	α_1	α_2
13	111	$11\bar{2}$	1	2
14	111	$\bar{2}11$	2	3
15	111	$1\bar{2}1$	3	1
16	$\bar{1}11$	$\bar{1}1\bar{2}$	4	5
17	$\bar{1}11$	$\bar{1}\bar{2}1$	5	6
18	$\bar{1}11$	211	6	4
19	$\bar{1}\bar{1}1$	$\bar{1}\bar{1}\bar{2}$	7	8
20	$\bar{1}\bar{1}1$	$2\bar{1}1$	8	9
21	$\bar{1}\bar{1}1$	$\bar{1}21$	9	7
22	$1\bar{1}1$	$1\bar{1}\bar{2}$	10	11
23	$1\bar{1}1$	121	11	12
24	$1\bar{1}1$	$\bar{2}\bar{1}1$	12	10

Table 2: {112} family of slip systems in BCC crystals and their corresponding conjugate pair (α_1 and α_2) of {110} systems given in table 1. Note that the crystallographic vectors $\boldsymbol{m}^{(\alpha)}$, $\boldsymbol{s}^{(\alpha)}$, $\boldsymbol{n}_1$ and $\boldsymbol{n}_2$ have to be normalized before their use.

Accepted manuscript

α/β	1	2	3	4	5	6	7	8	9	10	11	12	13	14	15	16	17	18	19	20	21	22	23	24
1	O	N	N	G	C	G	S	W	G	G	S	W	N	N	N	G	G	G	S	S	S	S	S	S
2	N	O	N	S	G	W	W	S	G	C	G	G	N	N	N	S	S	S	S	S	S	G	G	G
3	N	N	O	W	G	S	G	G	C	G	W	S	N	N	N	S	S	S	G	G	G	S	S	S
4	G	S	W	O	N	N	G	C	G	S	W	G	S	S	S	N	N	N	G	G	G	S	S	S
5	C	G	G	N	O	N	S	G	W	W	S	G	G	G	G	N	N	N	S	S	S	S	S	S
6	G	W	S	N	N	O	W	G	S	G	G	C	S	S	S	N	N	N	S	S	S	G	G	G
7	S	W	G	G	S	W	O	N	N	G	C	G	S	S	S	S	S	S	N	N	N	G	G	G
8	W	S	G	C	G	G	N	O	N	S	G	W	S	S	S	G	G	G	N	N	N	S	S	S
9	G	G	C	G	W	S	N	N	O	W	G	S	G	G	G	S	S	S	N	N	N	S	S	S
1	G	C	G	S	W	G	G	S	W	O	N	N	G	G	G	G	S	S	S	S	S	N	N	N
1	S	G	W	W	S	G	C	G	G	N	O	N	S	S	S	G	S	S	G	G	G	N	N	N
2	W	G	S	G	G	C	G	W	S	N	N	O	S	S	S	G	G	G	S	S	S	N	N	N
3	N	N	N	S	G	S	S	S	G	G	S	S	O	N	N	S	W	S	W	S	S	S	S	W
4	N	N	N	S	G	S	S	S	G	G	S	S	N	O	N	S	S	W	S	S	W	W	S	S
5	N	N	N	S	G	S	S	S	G	G	S	S	N	N	O	W	S	S	S	W	S	S	S	S
6	G	S	S	N	N	N	S	G	S	G	G	G	S	S	W	O	N	N	S	W	S	N	N	N
7	G	S	S	N	N	N	S	G	S	S	S	G	W	S	S	N	O	N	S	S	W	S	S	W
8	G	S	S	N	N	N	S	G	S	S	S	G	S	W	S	N	N	O	S	S	S	S	W	S
9	S	S	G	G	S	S	N	N	N	S	G	S	W	S	S	S	S	S	O	N	N	S	S	S
1	S	S	G	G	S	S	N	N	N	S	G	S	S	S	W	W	S	S	N	O	N	S	S	W
1	S	S	G	G	S	S	N	N	N	S	G	S	S	W	S	S	W	S	N	N	O	W	S	S
2	S	G	S	S	S	G	G	S	S	N	N	N	S	W	S	N	S	S	S	S	W	O	N	N
3	S	G	S	S	S	G	G	S	S	N	N	N	S	S	S	N	S	W	S	S	S	N	O	N
4	S	G	S	S	S	G	G	S	S	N	N	N	W	S	S	N	W	S	S	W	S	N	N	O

Table 3: Latent hardening (amplitude factor) matrix $q_{\alpha\beta}$ (Lee et al., 1999).

Accepted manuscript

ACCEPTED MANUSCRIPT

N	C	G	W	S
1	1	1	1.4	1.4

Table 4: Latent hardening coefficients (Lee et al., 1999).

C_{11} (MPa)	C_{12} (MPa)	C_{44} (MPa)
469.0E3	167.6E3	106.8E3

Table 5: Elastic moduli of molybdenum single crystal (Bolef and Klerk, 1998).

$\Delta G_{k\circ}$	Activation enthalpy for kink pair nucleation	0.16568E-18 J
p and q	Parameters which define thermal barrier shape	0.5 and 1.25
$\tau_\circ$	Resolved yield stress at 0 K	665 MPa
$g_\circ$	Initial athermal slip resistance (CRSS)	2 MPa

Table 6: Material properties of molybdenum single crystal.

a_1	a_2	a_3	a_4	a_5
0.24	0.35	0.35	0.24	0.35

Table 7: Coefficients of non-Schmid stresses for molybdenum single crystal.

	$\langle 111\rangle\{110\}$	$\langle 111\rangle\{112\}$ AT	$\langle 111\rangle\{112\}$ TW
$g_\circ^\alpha$(MPa)	2.0	2.0	2.0
g_s^α (MPa)	20.0	15.0	15.0
$h_\circ^\alpha$ (MPa)	1500	2000	2000
h_s^α (MPa)	15.0	40.0	40.0

Table 8: Material properties of molybdenum single crystal. AT and TW represents anti-twinning and twinning sense, respectively.

Accepted manuscript

ACCEPTED MANUSCRIPT

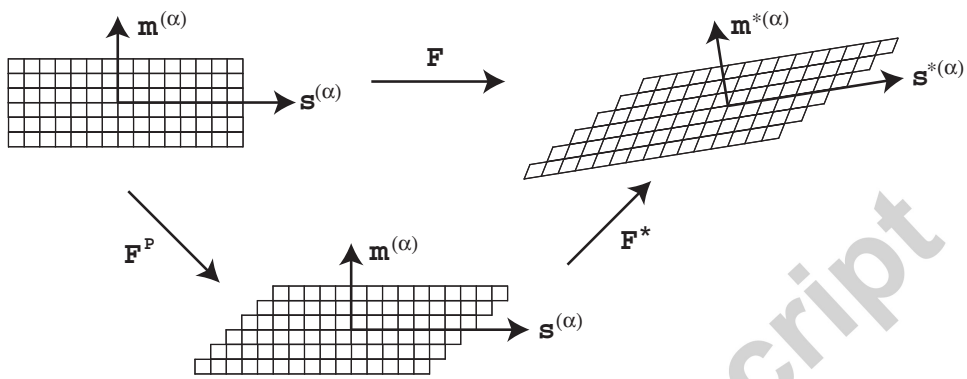

Figure 1: Basic geometric assumption of macroscopic single crystal plasticity.

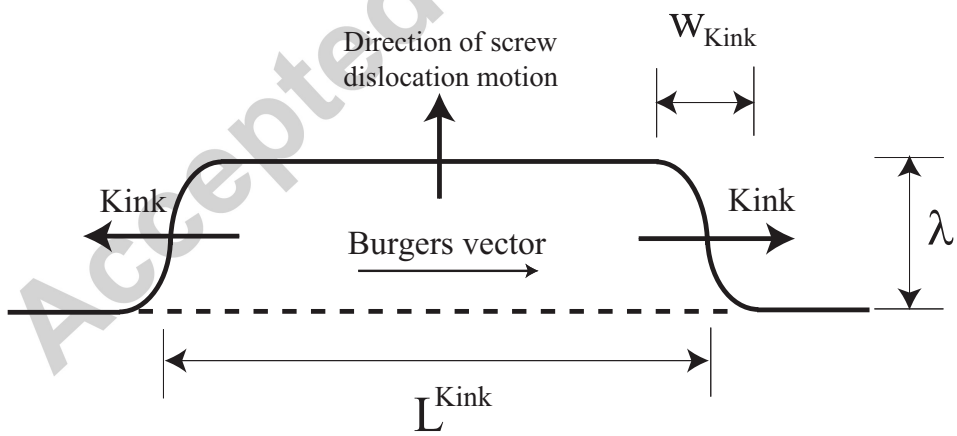

Figure 2: Schematic showing motion of screw dislocation by the nucleation and propagation of kink pairs.

Accepted manuscript

ACCEPTED MANUSCRIPT

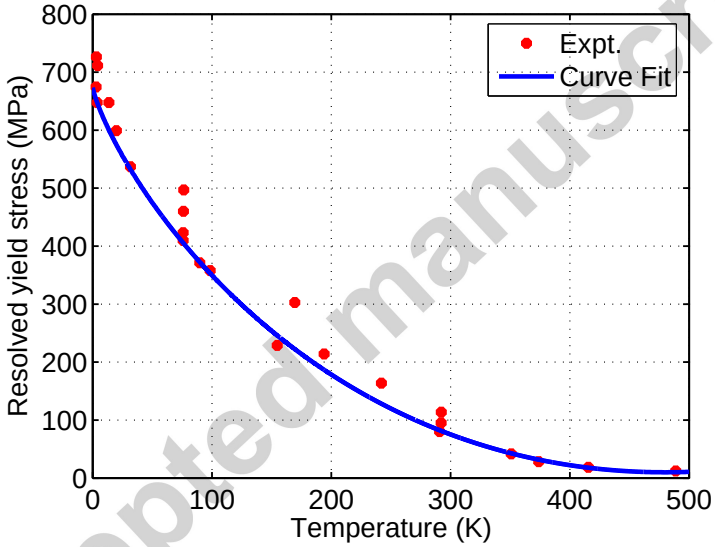

Figure 3: The critical resolved shear stress for Mo single crystal as a function of temperature (Kaufmann et al., 1984).

Accepted manuscript

ACCEPTED MANUSCRIPT

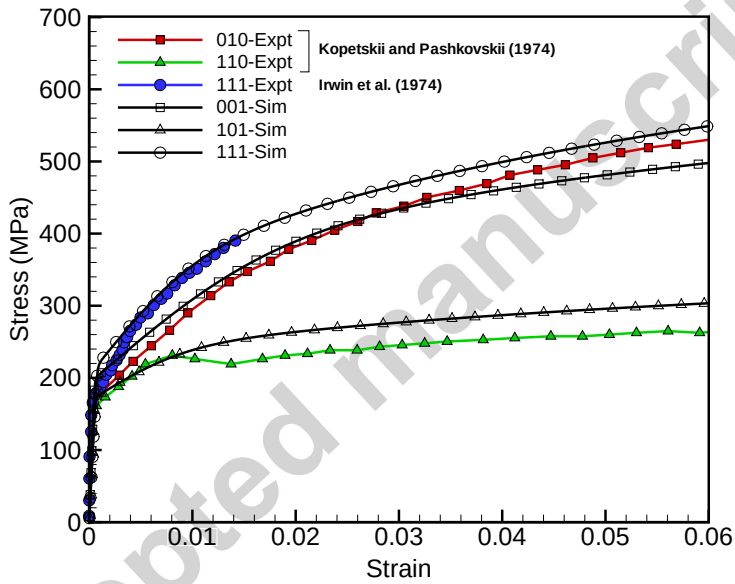

Figure 4: The experimental and simulated stress versus strain curves obtained from uniaxial tension test carried out at 293 K, with a strain rate of 6.0E-5 s^{-1} and for orientations such that [010], [111] and [101] are along tensile axis. Experimental data is from (Irwin et al., 1974) and (Kopetskii and Pashkovskii, 1974)

Accepted manuscript

ACCEPTED MANUSCRIPT

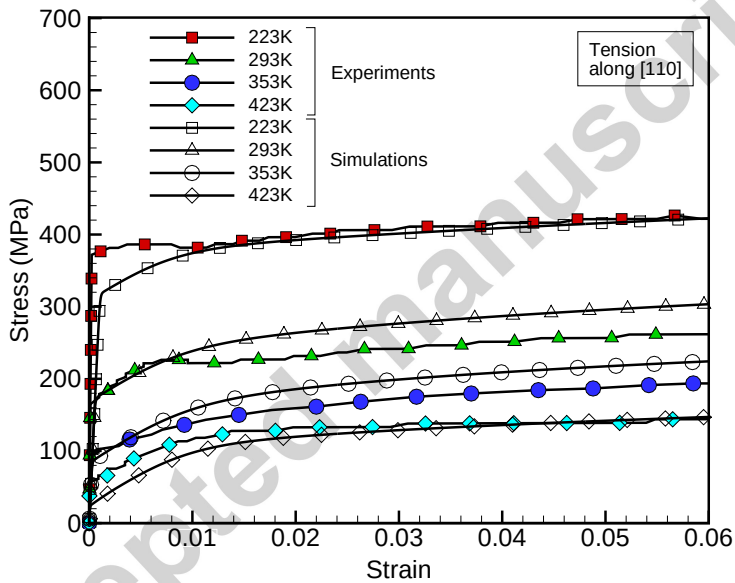

Figure 5: The resolved shear stress versus strain curves obtained from uniaxial tension test carried out at different temperatures, with a strain rate of 6.0E-5 s^{-1} and for orientations such that [101] is along tensile axis.

Accepted manuscript

ACCEPTED MANUSCRIPT

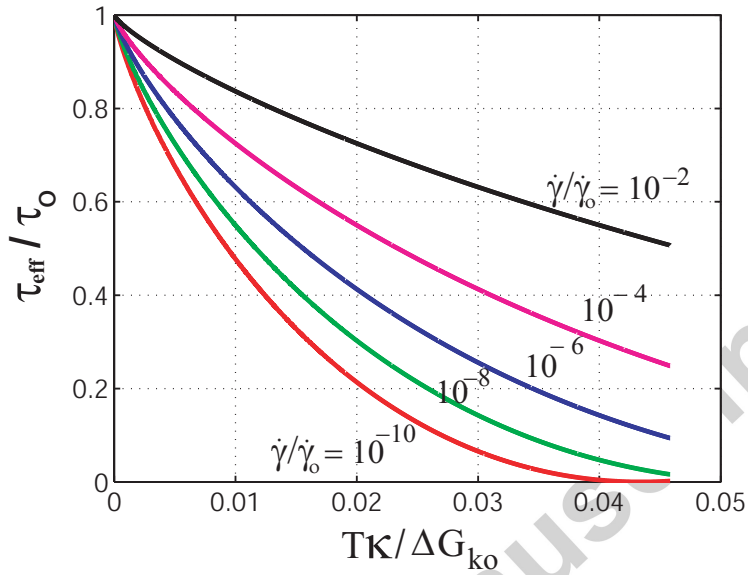

Figure 6: The temperature dependence of effective resolved shear stress for various strain rates. Note the typical order of $\dot{\gamma}_\circ \approx 10^6 s^{-1}$ and $\tau_\circ = 665$ MPa (Kaufmann et al., 1984)

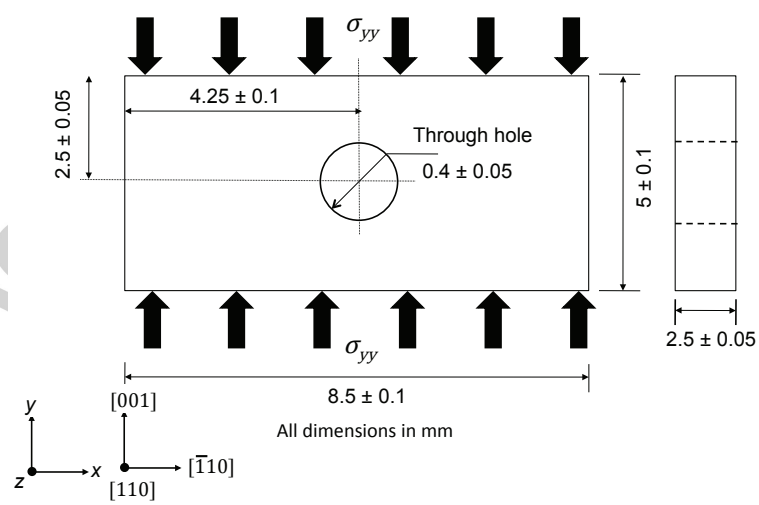

Figure 7: Schematic of Molybdenum single crystal orientation, specimen geometry and locading conditions used in uniaxial compression experiment

ACCEPTED MANUSCRIPT

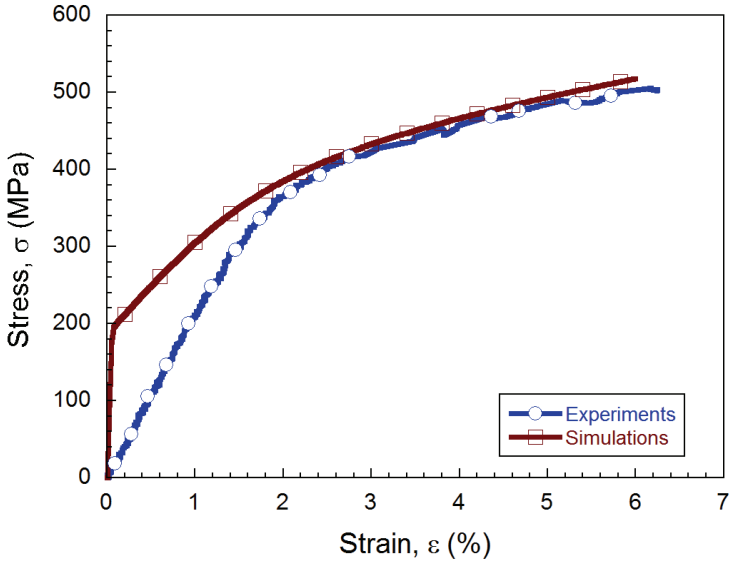

Figure 8: Comparison of prediction stress-strain response in compression from numerical simulation and measured response from an experiment of single crytal Mo with a hole under uniaxial compression.

ACCEPTED MANUSCRIPT

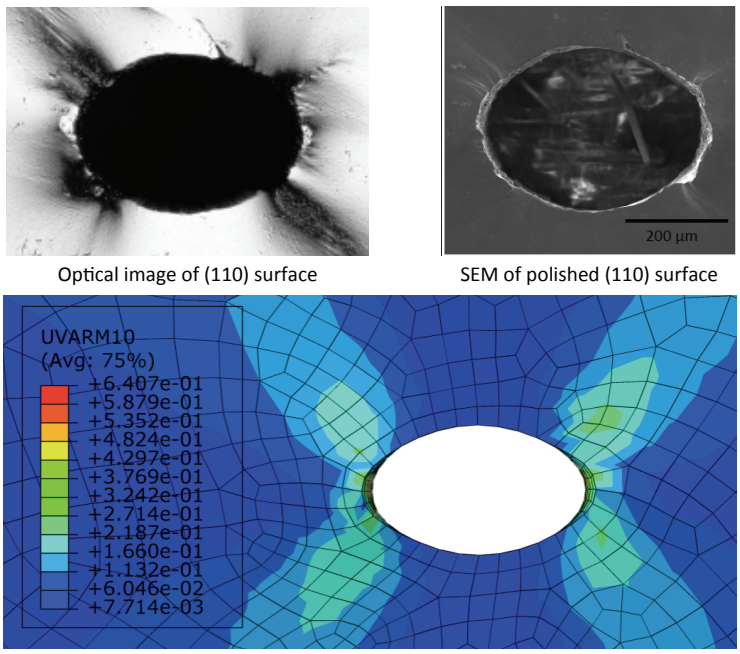

Figure 9: Qualitative comparison of predicted localization of plastic strains from numerical simulation and evidence of localzation from deformed specimen using optical microscopy of virgin surface and SEM of polished surface.

ACCEPTED MANUSCRIPT

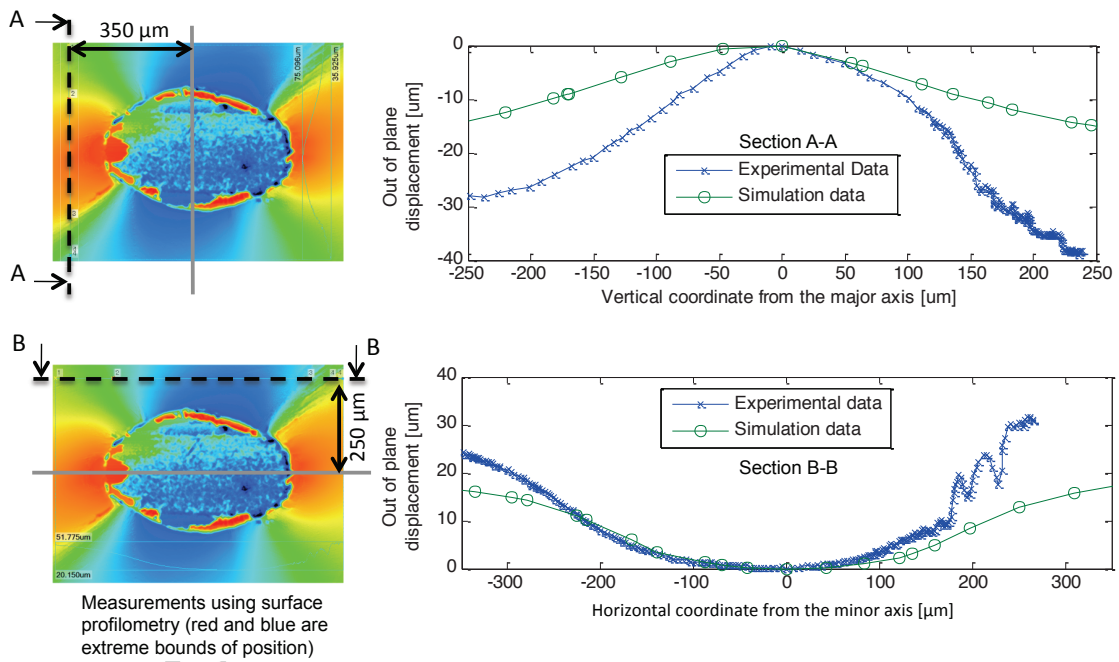

Figure 10: Comparison of predicted out-of-plane displacements from numerical simulation and measured response using a surface profilometer on a deformed specimen.